Aust. J. Phys., 1985, **38**, 471–86

The Anatomy of an Image*

A. F. Moodie and H. J. Whitfield

Division of Chemical Physics, CSIRO,
P.O. Box 160, Clayton, Vic. 3168.

Abstract

Following the approach employed by Mathieson in his analysis of an X-ray Bragg reflection, we dissect the images of the 3, 3 polymorph of CuAsSe and show that certain characteristic patterns which outline the structure are to be found in the lattice images of a wide range of tetrahedrally bonded species.

1. Introduction

Whether an image can be interpreted intuitively depends on the optical system and on the nature of the interaction between the object and the illuminating radiation. In conventional microscopy the conditions on the interaction are that the object should modify the wavefield only by absorption, and pictorially, that the probability of scattering more than once within the object should be negligible. Neither of these conditions is satisfied in the scattering of electrons by matter.

In general, then, the interpretation of electron micrographs is not a straightforward matter, but for certain classes of compounds general patterns can sometimes be discerned so that trial structures can be postulated. Well-known methods can then be used to calculate images and diffraction patterns, and hence refine the initial estimate.

It is the purpose of this communication to dissect the images obtained from a compound of known structure, namely the 3, 3 (or hcchcc) polytype of CuAsSe, in order to reveal the patterns common to that range of structure based on the stacking of tetrahedrally bonded species.

2. Outline of the Theory

The complexity of lattice images derives from the strength of the coupling of the electron to the potential within the object, a coupling which is some three orders of magnitude greater than that for electromagnetic radiation. Approximations on which, for instance, the design of the phase-contrast microscope and the procedures used in X-ray structure analysis are based are then no longer valid.

* Dedicated to Dr A. McL. Mathieson on the occasion of his 65th birthday.

0004-9506/85/030471$02.00

The theoretical treatment adequate to calculate images and diffraction patterns to substantially arbitrary accuracy is well known, but an outline of one approach will be given as a means of summarizing various approximations which will be used below. This approach is a transcription of standard one body scattering theory, and has some shortcomings for a crystallographer, but is chosen in this instance because it is set in the direct space of the image rather than the momentum space of the diffraction pattern.

The elastic scattering of electrons can be described by a Klein–Gordon equation,

$$\nabla^2\psi + \frac{8\pi^2 m|e|\phi}{h^2}\psi + \frac{8\pi^2 m_0|e|W}{h^2}\left(1 + \frac{|e|W}{2m_0 c^2}\right)\psi = 0.$$

Here W is the accelerating voltage and ϕ the potential in the crystal is defined as being positive. The relativistic values for mass and wavelength are given by

$$m = m_0(1 - v^2/c^2)^{-\frac{1}{2}}, \qquad \lambda = h\{2m_0|e|W(1 + |e|W/2m_0 c^2)\}^{-\frac{1}{2}}.$$

More compactly, we have

$$\nabla^2 + k^2(1 + \phi/W)\psi = (\nabla^2 + k^2 + 2k\sigma\phi)\psi = 0, \tag{1}$$

where

$$\sigma = \frac{\pi}{W\lambda}\,\frac{2}{1+(1 - v^2/c^2)^{\frac{1}{2}}}.$$

For fast electrons ϕ/W is a slowly varying function on a scale of wavelength and is small compared with unity. The scattering will therefore be peaked about the direction defined by the incident beam and simplification is possible.

By an intuitive method it can be argued that since $\phi/W \ll 1$, then the component of the motion along z is little changed by scattering. Hence, making the substitution $\psi = \psi\exp(\mathrm{i}\,k_z z)$, neglecting $\partial^2\psi/\partial z^2$ and taking the object to be in the form of a plate normal to the z-axis, equation (1) becomes

$$\frac{\partial\psi}{\partial z} = \mathrm{i}\left(\frac{1}{2k_z}(\nabla^2_{x,y} + K_0^2 + \sigma\phi)\right)\psi, \tag{2}$$

where $\nabla^2_{x,y} = \partial^2/\partial x^2 + \partial^2/\partial y^2$, $K_0 = k_x + k_y$ is the transverse wave vector and $\psi(x, y, 0) = \exp\{\mathrm{i}(k_x x + k_y y)\}$. Equation (2) is in the form of a time dependent Schrödinger equation, so that the theory of the evolution operator can be directly invoked. [A recent account has been given by Gratias and Portier (1983).]

In terms of the Hamiltonian of the two-dimensional system,

$$-H(z) = (1/2k_z)(\nabla^2_{x,y} + K_0^2) + \sigma\phi,$$

the evolution operator $U(z, z_0)$ defined by

$$\psi(z) = U(z, z_0)\psi_0$$

satisfies

$$\mathrm{i}\,\partial\, U(z, z_0)/\partial z = H(z)\, U(z, z_0)$$

or

$$U(z, z_0) = 1 - \mathrm{i} \int_{z_0}^{z} U(z, z_1)\, H(z_1)\, \mathrm{d}z_1 . \tag{3}$$

At the gaussian focus of a perfect electron microscope the contrast will, of course, be uniform and this is made explicit in equation (3). This equation can be solved iteratively by direct computation and the terms collected in ascending order of interaction to give a Born series, essentially in powers of $\sigma\phi$ and the differentials of ϕ. Since in the voltage range routinely used in microscopy $\sigma\phi$ is of order 10^{-3} Å^{-1}, the series will converge very slowly for nearly all practical cases. Numerical values must therefore be obtained by other methods.

So far we have assumed ϕ to be a function of x, y and z. When the periodicity in the z direction is not too great however, the dependence on z may be neglected and the solution simplifies to give

$$\begin{aligned} U(z, z_0) &= 1 - \mathrm{i} H(z - z_0) + (\mathrm{i}^2/2!) H^2(z - z_0) - \ldots \\ &= \exp\{-\mathrm{i}\, H(z - z_0)\} . \end{aligned} \tag{4}$$

This is a sufficiently good approximation to describe most images at least in outline, but in preliminary evaluation even simpler forms are required. If the object is sufficiently thin and the wavelength short, the terms involving differentials become small and the phase grating approximation is obtained as

$$\psi = \exp(\mathrm{i}\,\sigma\phi z)\psi_i . \tag{5}$$

At small defects of focus the intensity distribution then approximates to the charge density (Lynch *et al.* 1975) and intuitive interpretation is possible.

The first Born approximation results from selecting only those terms that are first order in $\sigma\phi$. The range of validity is very limited. If the object is crystalline the series can be summed to give

$$\psi = 1 + \mathrm{i} \sum_g V(g) \frac{\sin\{\pi\zeta(g) z\}}{\pi\zeta(g)} \exp(2\pi\, \mathrm{i}\, \boldsymbol{g}.\boldsymbol{r}),$$

where the excitation error

$$\zeta(g) = \{K_0^2 - (K_0 + g)^2\}/4\pi k_z$$

measures the deviation from the Bragg condition and derives directly from the operation of the kinetic energy term in the Hamiltonian. Dynamical results are usually expressed in terms of the excitation errors, and this is appropriate in reciprocal space. In image space, however, qualitative assessments can sometimes be made more directly in terms of the differentials.

The third type of approximation used in this paper involves the summation of all orders of interaction for a limited number of beams. The prototype is the two beam approximation in which the intensity of the forward scattered beam has a cos-squared dependence on thickness and is complementary to the diffracted beam. Analogous

wavefunctions are generated at symmetric orientations to a few strongly coupled beams (Niehrs 1959).

None of these approximations is, by itself, adequate to describe the images generated by the more complicated chalcogenides. Experimental data were therefore collected from a typical compound of known structure.

3. Experimental

The method of preparation and the determination of the crystal structure by single crystal X-ray diffraction of the 3, 3 or hcchcc polymorph of CuAsSe has been reported previously (Whitfield 1981).

Specimens of CuAsSe suitable for high-resolution electron microscopy were prepared by crushing crystals in an agate mortar under ethanol. The thin crystals were deposited on holey carbon films and examined in a JEOL 200CX electron microscope in a configuration (Moodie and Whitfield 1984) that allowed direct switching between convergent beam electron diffraction (CBED) and imaging of the field at ultra-high resolution.

We describe elsewhere (Glanvill *et al.* 1985) how we use optical diffractograms of a through focus series of amorphous films of C, Si and Ge to determine the spatial frequencies of maximum and minimum phase contrast, and thence the spherical aberration coefficient C_s of the JEOL 200 kV electron microscope. In the particular configuration we used, with a tilting stage holder placed very low in the objective lens and with a double-gap condenser, the measured spherical aberration is 0·94 mm.

Lattice images were calculated using the multi-slice formulation of the dynamical theory for electron diffraction (Cowley and Moodie 1957). The calculations were carried out using special purpose computer programs written by D. Lynch.

Table 1. Atomic coordinates for ideal and actual structure of CuAsSe

Atom	Ideal			Actual		
	x	y	z	x	y	z
As(1)	0·0000	0·0000	0·1875	0·0156	0·0108	0·1806
As(2)	0·0000	0·3333	0·3542	0·0168	0·3580	0·3541
As(3)	0·0000	0·3333	0·0208	0·0176	0·3229	0·0170
Se(1)	0·1667	0·5000	0·1875	0·1645	0·4773	0·1803
Se(2)	0·1667	0·8333	0·3542	0·1636	0·8701	0·3455
Se(3)	0·1667	0·8333	0·0208	0·1646	0·8100	0·0144
Cu(1)	0·8333	0·5000	0·1875	0·8315	0·5364	0·1965
Cu(2)	0·8333	0·8333	0·3542	0·8343	0·8151	0·3598
Cu(3)	0·8333	0·8333	0·0208	0·8265	0·8644	0·0307

4. Structure of hcchcc–CuAsSe

The compound CuAsSe crystallizes in the orthorhombic space group *Pbcn* with $Z = 24$ in a unit cell of dimensions $a = 11{\cdot}75$, $b = 6{\cdot}79$ and $c = 19{\cdot}21$ Å, and with all atoms in general 8-fold positions (Whitfield 1981). This structure is related to the B6 structure of the 6H polytype of ZnS but all three kinds of atoms (Cu, As and Se) occupy the equipoints of the 6H ZnS lattice in such a way that each Cu is coordinated by 1As+3Se, each As by 1Cu+2As+1Se, and each Se by 1As+3Cu. The Cu–As, Cu–Se and As–Se bond lengths are appreciably different and there is an associated distortion from perfect tetrahedral angles of 109°28′.

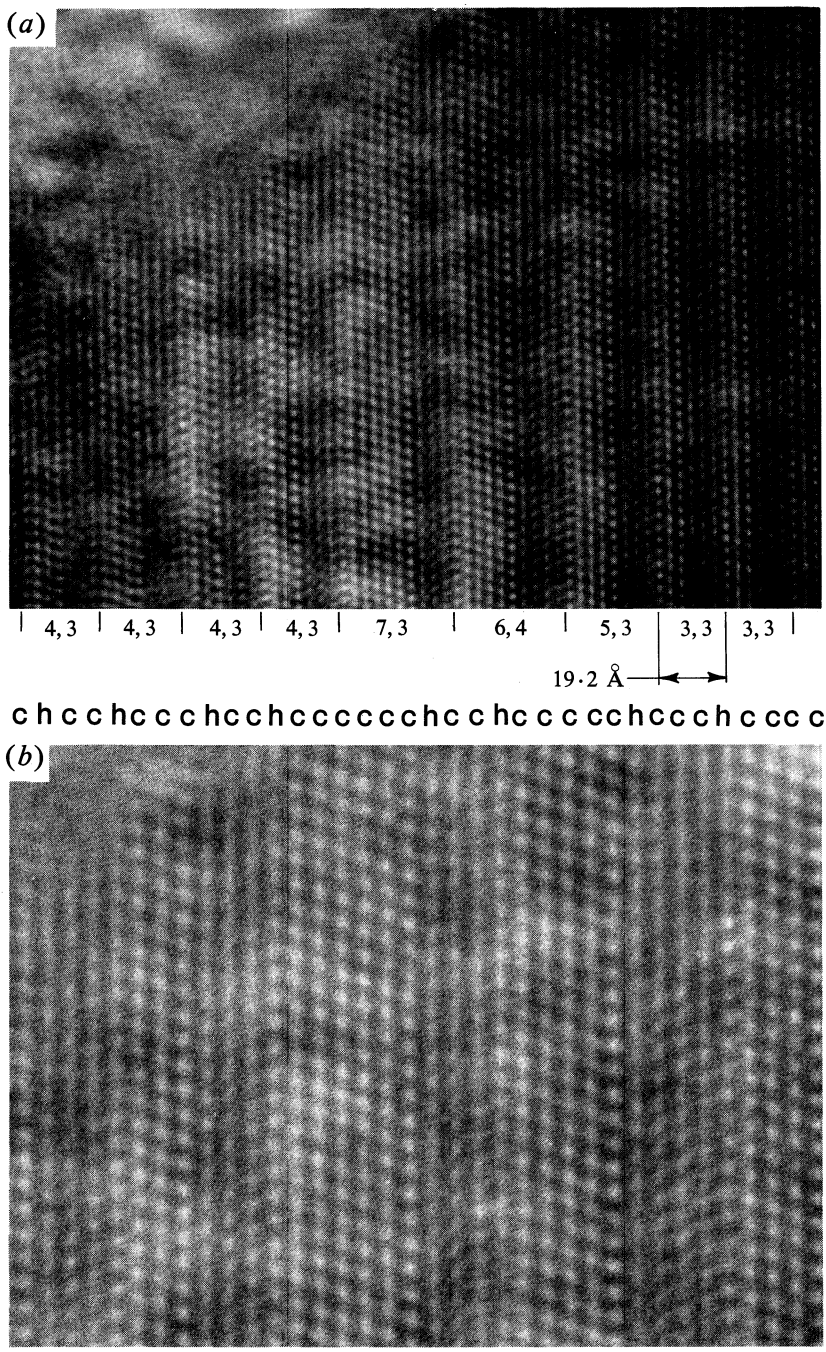

Fig. 1. (*a*) Experimental image of a mixture of polytypes of CuAsSe. To the left of the crystal is the 4, 3 polytype, to the right of the crystal is the 3, 3 polytype, and in the centre are observed stacking patterns 7, 3 6, 4 and 5, 3. (*b*) Enlargement of the centre portion of (*a*) with the stacking sequence indicated.

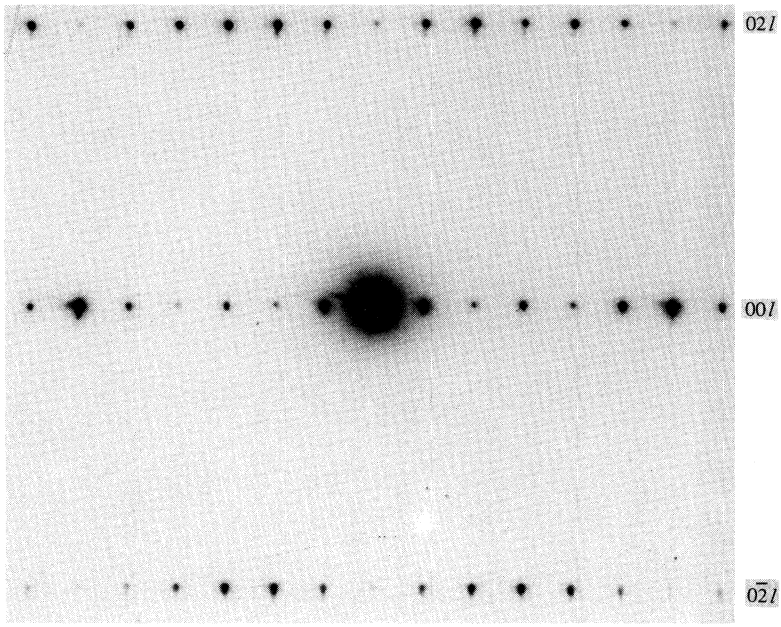

Fig. 2. Selected area diffraction pattern of the $0kl$ projection of hcchcc–CuAsSe viewed down the [100] direction. Note that the $00l$ reflections with l odd, forbidden in appropriate orientation (see Figs 3 and 4), are quite strong. This results from the averaging over angle, deriving both from residual convergence in the illuminating system and bends in the crystal.

There is a simple relationship between the lengths of the three axes of CuAsSe, namely $a/\sqrt{3} = b = c/\sqrt{8}$. For an 'ideal' CuAsSe structure in which this relation between unit cell lengths is exact and with perfect tetrahedral coordination with equal bond lengths for Cu–As, As–As, Cu–Se and As–Se, the atomic coordinates of the atoms in the asymmetric unit of CuAsSe would be

$$\begin{array}{llll} \text{As} & (0, 0, \tfrac{9}{48}) & (0, \tfrac{1}{3}, \tfrac{17}{48}) & (0, \tfrac{1}{3}, \tfrac{1}{48}), \\ \text{Se} & (\tfrac{1}{6}, \tfrac{1}{2}, \tfrac{9}{48}) & (\tfrac{1}{6}, \tfrac{5}{6}, \tfrac{17}{48}) & (\tfrac{1}{6}, \tfrac{5}{6}, \tfrac{1}{48}), \\ \text{Cu} & (\tfrac{5}{6}, \tfrac{1}{2}, \tfrac{9}{48}) & (\tfrac{5}{6}, \tfrac{5}{6}, \tfrac{17}{48}) & (\tfrac{5}{6}, \tfrac{5}{6}, \tfrac{1}{48}). \end{array}$$

In Table 1 these atomic coordinates for the 'ideal' structure are compared with the experimentally determined coordinates.

At the resolutions attainable in the JEOL 200CX the most informative projection is likely to be $[0kl]$ which, in effect, displays the stacking sequence (see Fig. 1).

5. Images

The $[0kl]$ projection was identified by its diffraction pattern (see Figs 2–4), and through focal series of images were obtained for a range of thicknesses (Fig. 5). At negative defect of focus three main types of contrast distribution could be distinguished; namely, with white patches in the approximate positions of the 'holes' (Fig. 5*a*), with white patches in the approximate positions of the pairs of atoms (Fig. 5*b*), and with undulating symmetrical lines (Fig. 5*c*).

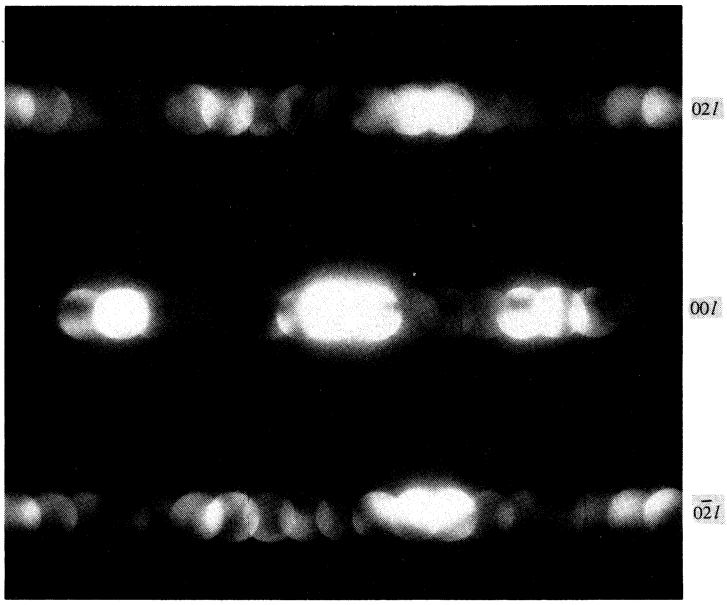

Fig. 3. CBED pattern of the $0kl$ projection of hcchcc–CuAsSe. The incident beam is tilted along the [001] direction of the crystal to satisfy the 001 beam. Note the sharpness of the black bands in the odd orders of $00l$ and the high intensity outside these bands.

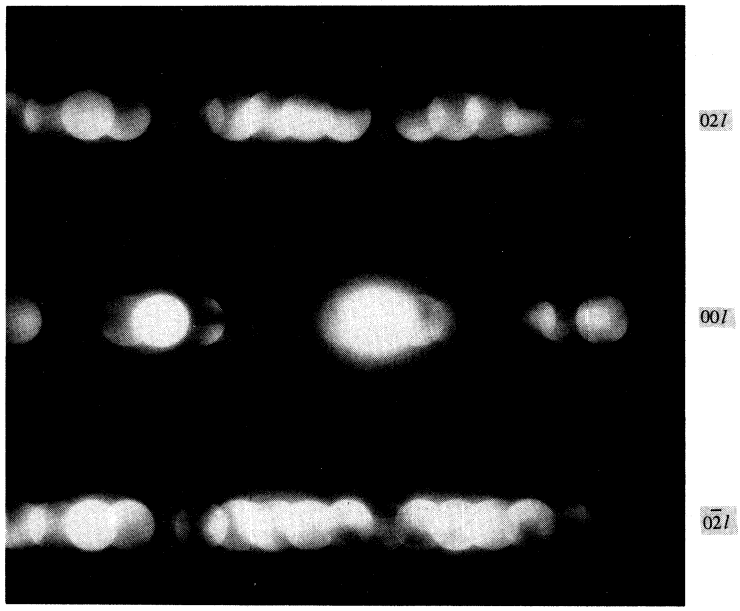

Fig. 4. CBED pattern of the $0kl$ projection of hcchcc–CuAsSe. The incident beam is tilted slightly along the [001] direction to satisfy the 005 beam. Note the cross on the fifth order beam.

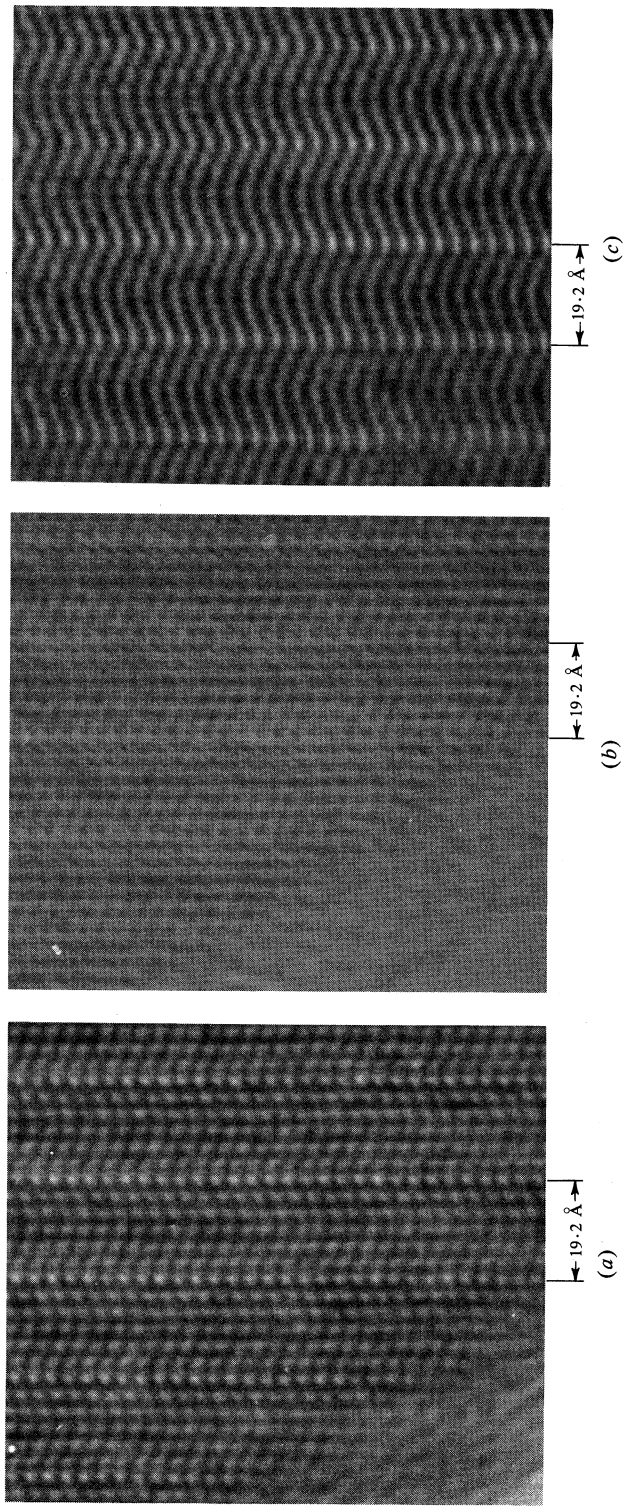

Fig. 5. Experimental images at different defects of focus of 3, 3 CuAsSe ($a = 11\cdot75$, $b = 6\cdot79$ and $c = 19\cdot2$ Å) viewed down the a-axis: (a) with white patches in the approximate positions of the 'holes', (b) with white patches in the approximate positions of the pairs of atoms and (c) with undulating symmetrical lines.

Table 2. Calculated intensities I and phases Φ for $00l$ and $02l$ thickness fringes of hcchcc–CuAsSe

Incident beam is along the [100] direction

	$z = 5a$		$z = 10a$		$z = 16a$		$z = 20a$	
$h\,k\,l$	I	Φ	I	Φ	I	Φ	I	Φ
0 0 0	0·488	32	0·082	−10	0·682	−14	0·724	15
0 0 2	0·000002	152	0·00007	−141	0·00002	51	0·00002	15
0 0 4	0·00003	−9	0·00007	81	0·00015	−146	0·00034	−72
0 0 6	0·0752	143	0·142	−166	0·0326	−103	0·0046	−82
0 0 8	0·00001	−140	0·00008	−86	0·00008	−10	0·00004	77
0 0 10	0·00007	−33	0·00005	41	0·00011	−149	0·00025	−88
0 0 12	0·0015	172	0·0052	−138	0·0054	−73	0·0021	−42
0 2 0	0·0004	136	0·0007	181	0·0004	−113	0·0002	−47
0 2 1	0·0099	146	0·0190	−158	0·0067	−80	0·0011	27
0 2 2	0·0188	−37	0·0372	12	0·0104	73	0·0003	−93
0 2 3	0·0064	135	0·0125	171	0·0056	169	0·0133	139
0 2 4	0·0013	−16	0·0056	55	0·0138	120	0·0130	146
0 2 5	0·0024	−25	0·0059	39	0·0054	116	0·0018	159
0 2 6	0·0001	142	0·0004	−169	0·0002	112	0·00005	−70
0 2 7	0·0048	143	0·0080	−166	0·0019	−86	0·0004	54
0 2 8	0·0124	−41	0·0189	3	0·0018	64	0·0021	−83
0 2 9	0·0110	134	0·0147	171	0·0009	165	0·0079	112

Table 3. Calculated structure amplitudes (V) for hcchcc–CuAsSe

$h\,k\,l$	V_R	$h\,k\,l$	V_R	$h\,k\,l$	V_R	$h\,k\,l$	V_R
0 0 0	14·524	0 2 1	2·587	0 2 6	0·305	0 2 8	−2·877
0 0 2	0·354	0 2 2	−3·545	0 0 8	−0·010	0 2 9	2·858
0 0 4	−0·143	0 2 3	2·080	0 0 10	−0·221	0 2 10	0·849
0 0 6	7·108	0 2 4	−0·817	0 0 12	0·485	0 2 11	−0·012
0 2 0	0·489	0 2 5	−1·177	0 2 7	1·758	0 2 12	0·122

A series of images was calculated at representative defects of focus and thickness (see Tables 2 and 3 and Fig. 6) using Lynch's version of the multislice program and incorporating instrumental parameters determined by optical interferometry. These calculations fit the observed images in outline, but there are a number of significant discrepancies. For instance the calculations, as they should, show a glide line, but in the images this element of symmetry is reduced to a plane of reflection. Nevertheless, convergent beam patterns taken from the same volume of the crystal as the images show bands of low intensity in the odd order $00l$ discs (Figs 3 and 4), so that the specimen in fact has glide symmetry to high accuracy in the $0kl$ projection (Gjønnes and Moodie 1965). This point will be discussed in Section 6. First, however, the origin of the main features of the images will be considered.

The Fourier transform of the $0kl$ projection, or of equivalent projections, in the many polytypes (four of which are shown in Fig. 7) can be envisaged in terms of the transform of the unit of six atoms in the [110] projection of the diamond lattice (Fig. 8). This unit generates a sublattice and since in the overall structure it has two

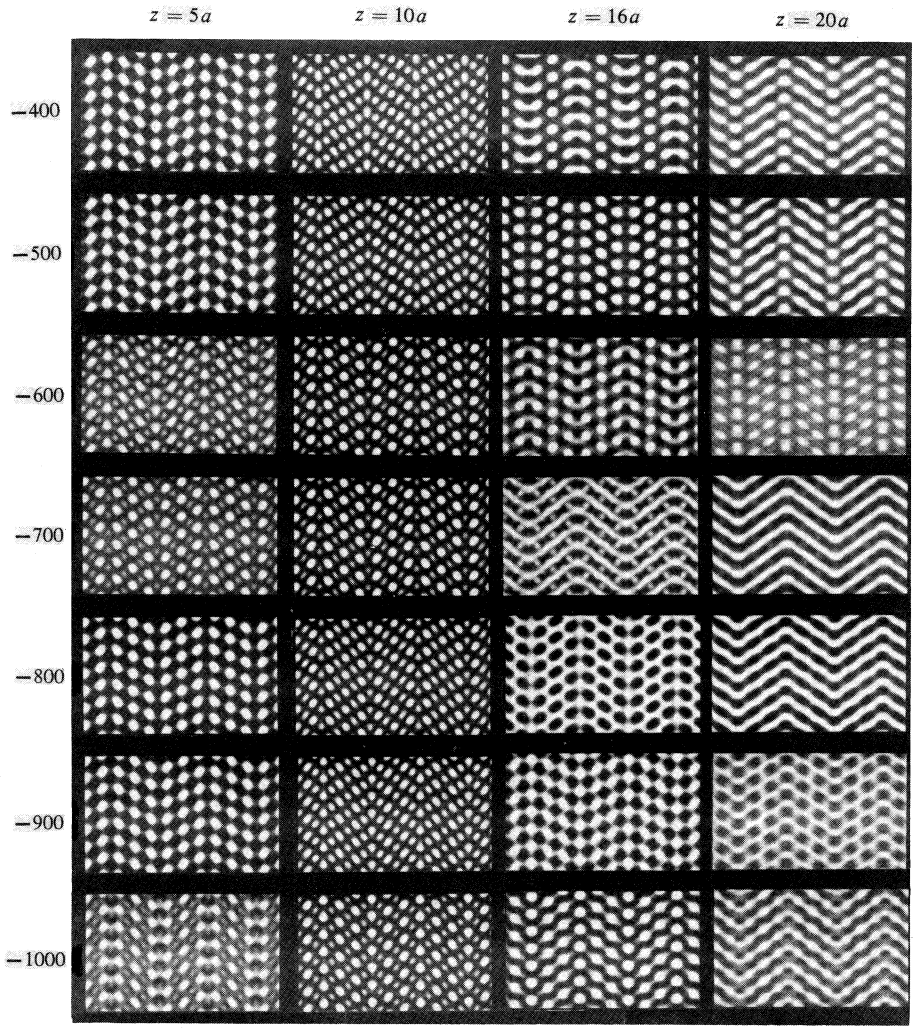

Fig. 6. Multislice calculations using $C_s = 0{\cdot}94$ mm of the 3, 3 (hcchcc) polytype of CuAsSe viewed down the a-axis ($a = 11{\cdot}75$ Å) with 200 kV electrons. Calculations are presented for seven defects of focus as indicated at the left of the diagram for each of four thicknesses $z = 5a$, $10a$, $16a$ and $20a$ as indicated at the top.

orientations, the transform of the projection has the typical appearance of a twin. The details of the superlattice convey in the standard way the details of the widths of the slabs of cubic material. This is illustrated in Fig. 9 which relates typical geometry to the characteristics of the electron microscope used in the experiments.

Suppose now that a crystal thin enough to satisfy the requirements of the charge density approximation is to be imaged. Then, defects of focus corresponding to curves e or f in Fig. 9 will be used. These curves give a qualitative indication of the resolution which can be expected, in this case, to be enough to resolve the lattice. And indeed, multislice calculations (see Fig. 6 for $z = 5a$; -400 and -500 Å) show a projection of the charge density with the atom positions black, and the holes, though not the

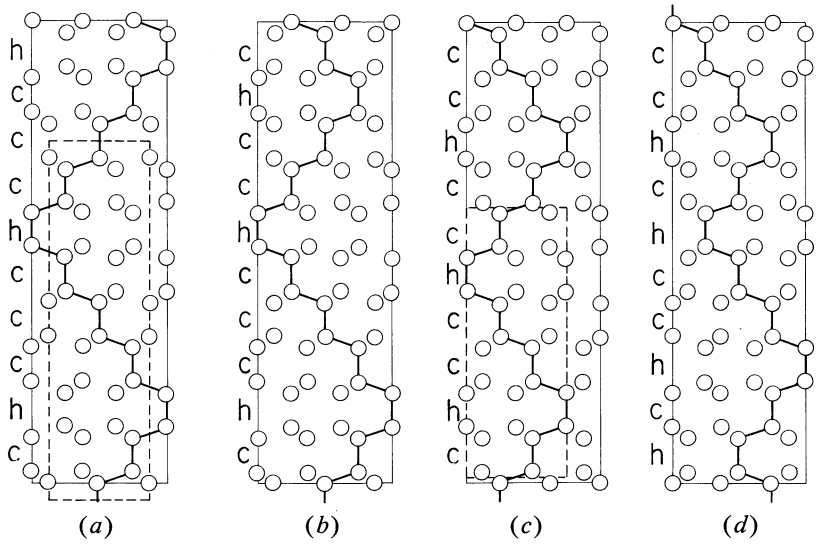

Fig. 7. Projections of ideal structures of the four different polytypes (*a*) hccchccc, (*b*) hccchcc, (*c*) hcchcc and (*d*) hcchc of CuAsSe with the unit cells of the 3, 3 (hcchcc) and 4, 4 (hccchccc) polytypes indicated by dashed lines.

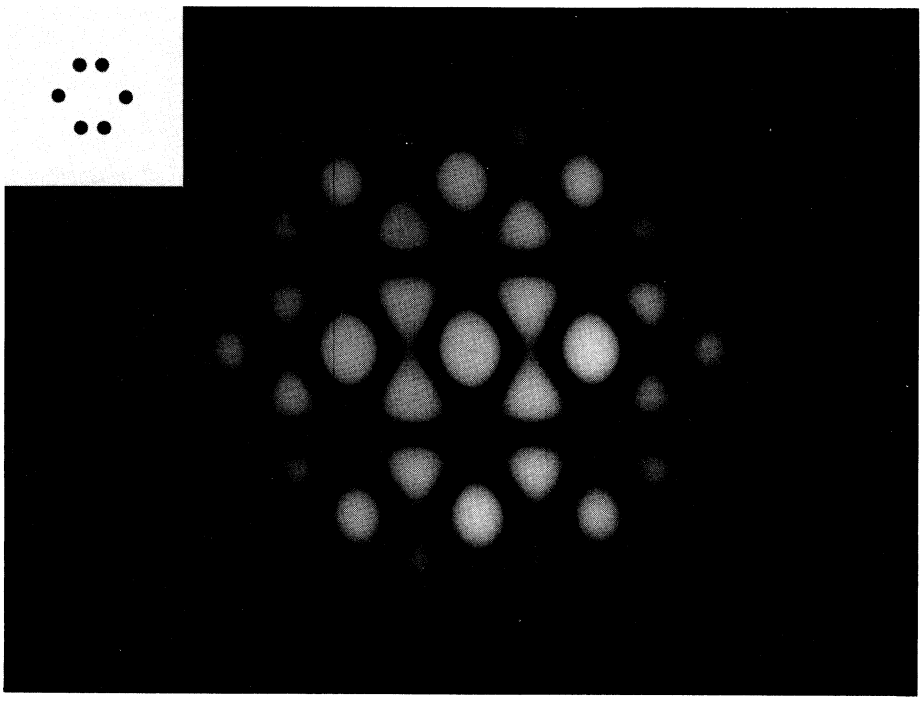

Fig. 8. Optical transform of the unit of six atoms in the [110] projection of the diamond lattice. The object is shown in the inset.

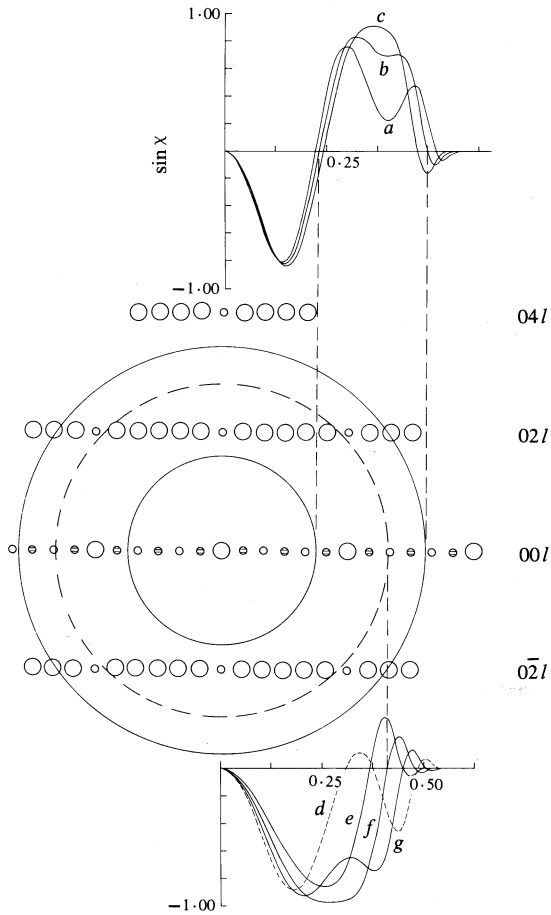

Fig. 9. Diagram of the CBED of hcchcc–CuAsSe with incident beam along the [100] direction showing intense beams as large circles, weak beams as small circles, and beams with dark bands (00 *l* for *l* odd) as shaded small circles. The transfer function sin χ of a 200 kV electron microscope with a spherical aberration of 0·94 mm is plotted as a function of distance in reciprocal space (Å^{-1}) for the various defects of focus (*a*) −950 Å, (*b*) −900 Å, (*c*) −850 Å, (*d*) −700 Å, (*e*) −400 Å, (*f*) −500 Å and (*g*) −600 Å.

individual atoms, resolved. In order to determine the stacking sequence however, it is sufficient to resolve the holes.

For the reasons given above, it is a characteristic of this type of compound that little intensity is scattered around the central beam. It is therefore plausible that a useful operating condition might be found at fairly large negative defect of focus. As can be seen from Fig. 9 curves *b* and *c*, corresponding to −900 and −850 Å defect of focus, generate an annular pass band which accepts more energy, apart from the central beam, than that for the charge density setting. The phase of the central beam is reversed with respect to the diffracted beams so that, qualitatively, a black to white

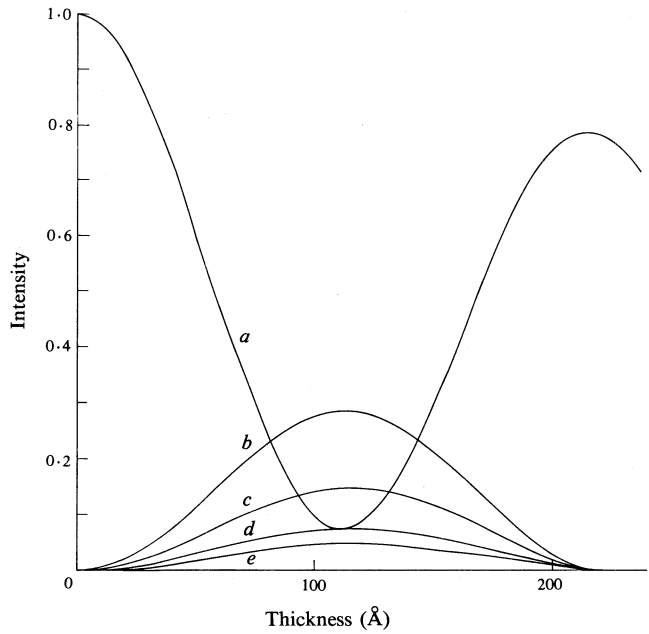

Fig. 10. Thickness fringes for (*a*) a central beam, (*b*) a 006 beam, (*c*) a 022 beam, (*d*) a 021 beam and (*e*) a 023 beam of hcchcc–CuAsSe (3, 3 polytype). The intensity of the 006 beam is multiplied by 2 and the intensities of the 021, 022 and 023 beams by 4.

reversal of contrast is to be anticipated, and this is, to good approximation found to be the case in quantitative calculations (see Fig. 6 for $z = 5a$; -800 and -900 Å).

In practice it is difficult to obtain crystals of these substances sufficiently thin to ensure the validity of the charge density approximation. In thicker crystals, interpretation of the image is simplified by the very small values of the low order structure amplitudes. This greatly reduces the coupling in the superlattice and between the superlattice and the sublattice. The low orders of the sublattice couple to form an effective two beam system (Niehrs 1959), the main effect of the weak beams being to damp the oscillations of the thickness fringes (see e.g. Anstis *et al.* 1974).

Precise calculations show that this approximation retains a high accuracy for all polytypes (see Fig. 10). The details of the extension of Niehr's work to cover the present and related cases will be the subject of a separate paper, but the outlines of the phenomenon can be briefly described in the Bloch wave picture.

When an orientation can be found in which all of the significant beams have nearly equal excitation errors and structure amplitudes, the magnitudes of all but two of the zero order components ${}^{j}t_0$ of the eigenvectors will, in turn, be very small. Since the wavefunction in momentum space can be written in terms of these quantities as (Fujimoto 1959)

$$U(h) = \sum_j {}^{j}t_h \, {}^{j}t_0^* \exp(2\pi \mathrm{i} \lambda_j z),$$

then $U(h)$ will collapse into an effective two beam form, and a perturbation series can be developed on the excitation errors, i.e. on the orientation.

Since, in an effective two beam form the intensity of the thickness fringe of the forward scattering beam is out of phase with the other diffracted beams, half periodicities increase in intensity as the central beam approaches extinction. In the present instance, the thickness at which this occurs is approximately 110 Å (Fig. 10) and the effect can be seen clearly in the calculations (see Fig. 6 for $z = 10a$ at all defects of focus).

At this thickness another complicating factor in the interpretation of the images becomes apparent. The zig–zag of high intensity, which is one of the most important structural features in this projection, depends quite sensitively on the balance in amplitude and phase between the 022 and the 023 beams, as an inspection of Table 2 shows. However, the phase difference between these beams is strongly dependent on thickness so that the zig–zag that has become most prominent is, in fact, structurally spurious.

Thus, at 200 kV and in a substance containing no element with an atomic number higher than 34, dynamical interaction is such that by a thickness of 100 Å an intuitive interpretation of the image would lead to a plausible, but completely erroneous structure.

However, the 000, 006, $00\bar{6}$, 022, $0\bar{2}\bar{2}$, $02\bar{2}$ and $0\bar{2}2$ reflections approximate an effective two beam system sufficiently closely for the overall pattern of images to begin, again, to resemble the structure as intensity flows back into the central beam. The contrast is, of course, reversed relative to that in the first half period. This correspondence is only approximate, largely because of the 021, 023 and 024 reflections. With increasing thickness the weight of the high order interactions of those beams with the effective two beam system induces excursions in phase and amplitude sufficient to perturb the images. At a defect of focus between -800 and -900 Å this perturbation is minimized by the shape of the transfer function, which reduces the weights of the 023 and 024 reflections relative to 022.

At a thickness of about 150 Å and at a defect of focus of about -900 Å, quite a close representation of the structure is obtained, holes being white. Most images have, in fact, been taken under these conditions since crystals of this thickness are readily obtained.

By 200 Å the equivalent two beam approximation is beginning to break down, the maximum in the intensity of the forward scattered beam being appreciably displaced from the minima of the other beams, which are nevertheless extremely weak. It would not be anticipated that the images would resemble the structure and, in fact, they are dominated by the zig–zags generated by the 023 and 024 reflections. The 006 reflection produces a detectable modulation of the zig–zag, but the effect of the 022 reflection is negligible except at -900 Å defect of focus, where the 023 and 024 reflections are substantially attenuated and an indistinct outline of the structure is generated. The two beam phase has again reversed, so that holes are black.

A further increase in thickness of 60 Å would bring the equivalent two beam cycle again into the range of the charge density approximation. This proves to be the case to an acceptable approximation for the 006 and 022 set, but the 023 and 024 group of reflections are now sufficiently strong, and sufficiently far from the two beam behaviour, that the image at -400 Å defect of focus—while a plausible subject for intuitive interpretation and while maintaining the 3, 3 character—is not a projection of the charge density. In particular, the angle of the zig–zag now dominated by the

023 reflections is incorrect, and the bright spots in each arm of the zig–zag lie too close to straight lines.

At greater thicknesses none of the known approximations have significant validity.

6. Effects of Tilt and Convergence of the Illuminating System

It has already been mentioned in Section 5 that the absence of glide symmetry in virtually all of the observed images constitutes the most serious of the discrepancies with the calculated distributions; further, convergent beam diffraction patterns derived from the same volume of crystal as the images show that the specimen in fact holds to glide symmetry with high precision. The same diffraction patterns (Figs 3 and 4) make clear that the reason for the lack of glide symmetry in most of the images is convergence in the illuminating beam, an effect also observed by Creek and Spargo (1985). Corrections of the standard type (O'Keefe and Sanders 1975) are of course included in the calculations. The additional corrections refer to reprojection of the structure, and the need for this can be most easily appreciated by an inspection of the odd orders of the $00l$ line of Figs 3 and 4.

The width of the band of low intensity through these orders provides an estimate of the angular range over which glide symmetry will be maintained to good approximation in the image. This width is a function of both thickness and structure, and it can be seen that in this structure the bands are narrow, even for thicknesses of a few hundred Ångströms.

Calculations carried out at small tilts reproduce the main observed effect, namely increased intensity at the peaks of the zig–zag (Fig. 5). With integration over angle a plane of reflection results.

Discrepancies at other thicknesses and other defects of focus can be accounted for similarly. For instance, the undulations referred to in Section 5 are very sensitive to tilt. In addition, the overall resolution is slightly reduced and this, again, is in accord with observation.

It is not implied here that the breakdown of glide symmetry is entirely or even largely due to nonzero amplitude on the zero layer line, but merely that the width of the band is diagnostic of the angular range for overall breakdown. In fact, the most important contributions come from the $02l$ and $0\bar{2}l$ lines.

The reasons for the smallness of the angular range derive from the large (11·75 Å) periodicity in the direction of the beam and in the distortions from the ideal diamond lattice, particularly round the arsenic atoms. In real space this results in large deviations from glide symmetry for small tilts, an effect which can be seen from a model and envisaged in terms of differentials of the potential. In reciprocal space the result can be understood in terms of the large structure amplitudes that can be linked in low order loops, so that there is cancellation for equality of the excitation errors, but large deviations for small differences in excitation errors.

In general, errors associated with tilted illumination will result in the loss of all symmetry in the image, an effect which can be readily explored with the microscope used in the present experiments. In the work described in this paper, although glide lines usually reduced to planes of symmetry, a complete loss of symmetry was never observed after careful alignment of the microscope. It is therefore concluded that, to the accuracy of the present experiments, beam misalignment does not lead to significant error.

7. Conclusions

The general outlines of the images of a range of tetrahedrally bonded chalcogenides can be understood in terms of a combination of the charge density and reduced two beam approximations. These reduced two beam approximations are likely to be of particular importance when reciprocal space has a pronounced substructure. Detailed agreement between calculated and observed images requires reprojection within the illuminating cone.

Acknowledgment

The authors thank Dr I. J. Wilson of the CSIRO Division of Chemical Physics for providing the optical transform shown in Fig. 8.

References

Anstis, G. R., Lynch, D. F., Moodie, A. F., and O'Keefe, M. A. (1974). *Acta Crystallogr.* A **29**, 138.
Cowley, J. M., and Moodie, A. F. (1957). *Acta Crystallogr.* **10**, 609.
Creek, R. T., and Spargo, A. E. C. (1985). *J. Appl. Crystallogr.* (in press).
Fujimoto, F. (1959). *J. Phys. Soc. Jpn* **14**, 1558.
Gjønnes, J., and Moodie, A. F. (1965). *Acta Crystallogr.* **19**, 65.
Glanvill, S. R., Moodie, A. F., Whitfield, H. J., and Wilson, I. J. (1985). *Aust. J. Phys.* (in press).
Gratias, D., and Portier, R. (1983). *Acta Crystallogr.* A **39**, 576.
Lynch, D. F., Moodie, A. F., and O'Keefe, M. A. (1975). *Acta Crystallogr.* A **31**, 300.
Moodie, A. F., and Whitfield, H. J. (1984). *Ultramicroscopy* **13**, 265.
Niehrs, H. (1959). *Z. Naturforsch.* **14a**, 504.
O'Keefe, M. A., and Sanders, J. V. (1975). *Acta Crystallogr.* A **31**, 307.
Whitfield, H. J. (1981). *J. Solid State Chem.* **39**, 209.

Manuscript received 11 February, accepted 16 April 1985